

Chapter 2

High-Strength Low-Alloy Steel

Abstract Growth kinetics of Widmanstätten austenite in ferrite in high-strength low-alloy steel is based on a model that describes diffusion controlled growth of precipitates with shapes approximating to needles or plates, where all the factors that may influence the precipitate growth, i.e. diffusion, interface kinetics and capillarity, are accounted for within one equation. The ratio between calculated and experimental values of the radius of the advancing tip is inversely proportional to the degree of supersaturation. Following this theoretical work, the tensile behaviour of high-strength low-alloy steel after tempering is discussed, and well explained in view of the interactions of mobile dislocations and dissolved carbon and nitrogen atoms and their effects on the strain hardening exponent. In the final section, splitting during fracture of tensile and impact loading is examined. Delamination does not occur in the as-rolled condition, but is severe in steel tempered in the temperature range of 500–650 °C. Steel that has been triple quench-and-tempered to produce a fine equiaxed grain-size also does not exhibit splitting. It is concluded that the elongated as-rolled grains and grain boundary embrittlement resulting from precipitates (carbides and nitrides) formed during reheating are responsible for the delamination.

2.1 Kinetics of the Diffusion-Controlled Ferrite to Widmanstätten Austenite Transformation

2.1.1 Growth Theory

2.1.1.1 Precipitate Plates and Needles

The equation relating the Peclet number (a dimensionless velocity parameter) $p = V\rho/2D$ to the dimensionless degree of supersaturation Ω_0 for the growth of plates is

$$\Omega_0 = \sqrt{\pi/p} \exp(p) \operatorname{erfc}(\sqrt{p}) \left[1 + \frac{V}{V_c} \Omega_0 S_1(p) + \frac{\rho_c}{\rho} \Omega_0 S_2(p) \right] \quad (2.1)$$

where V is the lengthening rate, D is the diffusion coefficient of solute in the matrix phase, erfc is the complementary error function, S_1 and S_2 are functions involved in the growth of plate. Other parameters can be calculated as below

$$\rho_c = \frac{\sigma v}{RT} \frac{1 - c_\alpha}{c_\beta - c_\alpha} \frac{c_\alpha}{c_0 - c_\alpha} \quad (2.2)$$

where σ is the interfacial free energy per unit area between precipitate and matrix, v is the molar volume of the precipitate, R is the gas constant, T is the temperature (in Kelvin), c_α is the solid solubility of the controlling element in the parent phase α , c_β is the concentration of the controlling element in the new phase β , c_0 is the concentration in the matrix before precipitation. The radius of curvature $\rho = 2f$, where f is the focal distance of the parabola of either plate or needle (Fig. 1.1c), defined uniquely for a parabola lengthening along the Z direction and thickening along the X direction. In Eq. 2.1, V_c is the velocity or the lengthening rate of a flat interface during interface controlled growth (i.e. when almost all the free energy is dissipated in the transfer of atoms across the interface so that the concentration difference in the matrix vanishes) and is given by

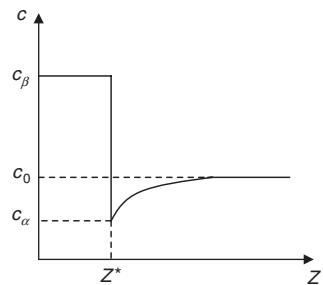
$$V_c = \mu_0 (c_0 - c_\alpha) \quad (2.3)$$

For curved interfaces, the growth rate is a function of the interface curvature via the Gibbs–Thomson effect. The curvature at which the growth rate becomes zero is $1/\rho_c$. The concentration parameters c_0 , c_α , and c_β are illustrated in Fig. 2.1. The values of functions $S_1(p)$ and $S_2(p)$ are given by Rivera–Díaz-del-Castillo and Bhadeshia (2001).

Equation 2.1 gives the general solution for the growth of precipitate plates. Note that the right-hand side is a sum of three terms of which the first term is for the case of the iso-concentration boundary. The second and the third terms are corrections to that solution due to the interface kinetics and capillarity effects respectively. The value of Ω_0 can be obtained from the phase diagram when the average composition of the alloy is known:

$$\Omega_o = \frac{c_0 - c_\alpha}{c_\beta - c_\alpha} \quad (2.4)$$

Fig. 2.1 Concentrations at precipitate boundary ($Z = Z^*$) for flat interface (From Guo and Sha (2004))
© Carl Hanser Verlag, Muenchen)



Equation 2.1 reveals that, for a given value of Ω_0 , multitudes of exact solutions are possible for the growth rate depending upon the value of the radius of curvature. The experimental observation that a plate grows at a constant rate indicates that a steady-state diffusion field exists with respect to the advancing interface and that the tip radius ρ remains unchanged during the growth. This implies that of many solutions available only one solution is stable with respect to small perturbation in the radius of curvature of the tip of the plate. This solution corresponds to the maximum growth rate. This maximum growth rate can be obtained by differentiating Eq. 2.1 with respect to ρ and setting $\partial V/\partial \rho = 0$, which gives us another relationship between Ω_0 , V , and ρ . The simultaneous solution of this equation with Eq. 2.1 then gives us unique values for V and ρ for a given value of Ω_0 .

The equation relating the Peclet number to the dimensionless supersaturation Ω_0 for the growth of needles is

$$\Omega_0 = p \exp(p) E_1(p) \left[1 + \frac{V}{V_c} \Omega_0 R_1(p) + \frac{\rho'_c}{\rho} \Omega_0 R_2(p) \right] \quad (2.5)$$

where E_1 is the exponential integral function, R_1 and R_2 are functions involved in the growth of needle, and ρ'_c is the critical radius of curvature for nucleation for a needle which is equal to twice that for a plate. The values of functions $R_1(p)$ and $R_2(p)$ have been given by Rivera-Díaz-del-Castillo and Bhadeshia (2001). Equation 2.5 gives the general solution for the growth of needles. The right-hand side is a sum of three terms of which the first is where interface kinetics and capillarity are neglected. The second and third terms account respectively for those effects. For a given value of Ω_0 , though many solutions are available only one is stable. This solution corresponds to the maximum growth rate. This maximum growth rate can be obtained by differentiating Eq. 2.5 with respect to ρ and setting $\partial V/\partial \rho = 0$, which gives us another relationship between Ω_0 , V , and ρ . The simultaneous solution of the resulting equation with Eq. 2.5 then gives unique values for V and ρ for a given value of Ω_0 . Growth theory for plate growth follows similar formulas and can be referred to from the earlier part of this section.

2.1.1.2 Approximation for the Growth of Needles or Plates

At a given supersaturation degree, the values of p and ρ/ρ'_c were given by Rivera-Díaz-del-Castillo and Bhadeshia (2001). Especially when the supersaturation is small, the values of p and ρ/ρ'_c approach asymptotically to simple relationships between p and Ω_0 . For needles, one has

$$\Omega_0 = \frac{2p[\ln(\kappa p)]^2}{1 - \ln(\kappa p)} \quad (2.6a)$$

$$\frac{\rho}{\rho'_c} = -\frac{3.841}{4} \frac{\Omega_0 \ln(\kappa p)}{\Omega_0 + p \ln(\kappa p)} \quad (2.6b)$$

where $\kappa = \exp(-\gamma)$, γ being the Euler constant ($\gamma = 0.57722\dots$).

Simplified kinetic expressions for the growth of precipitate plates are:

$$p = \frac{9}{16\pi} \Omega_*^2 \quad (2.7a)$$

$$\frac{\rho}{\rho_c} = \frac{32}{3} \frac{1}{\Omega_*} \quad (2.7b)$$

where the corrected degree of supersaturation (dimensionless)

$$\Omega_* = \frac{\Omega_0}{1 - \frac{2}{\pi} \Omega_0 - \frac{1}{2\pi} \Omega_0^2} \quad (2.8)$$

The above-simplified expressions are valid even when p is up to 1 or Ω_0 to 0.85. The final lengthening rate expression can be obtained by using the definition of the Peclet number, which results in:

$$V = \frac{9}{8\pi} \frac{D}{\rho} \Omega_*^2 = \frac{27}{256\pi} \frac{D}{\rho_c} \Omega_*^3 \quad (2.9)$$

where D is the diffusion rate of alloying elements in the ferrite matrix. These expressions are simple and show clearly the dependence of radius of curvature and growth rate on the degree of supersaturation.

2.1.2 Parameter Determination and Calculation

The ferrite-to-Widmanstätten austenite transformation in high-strength low-alloy (HSLA) Fe–C–Mn–Nb steel is studied using this theory with experimental values of the radius of the advancing tip. The chemical composition of the steel is Fe-0.693C-1.514Mn-0.022Nb-0.028N-0.178Si-0.047Al (at.%), referred to as Nb-steel.

The specimens were encapsulated in quartz tubes under vacuum and solution treated at 1500 K for 2 h. They were then isothermally transformed at 923 K for 30 min and quenched to obtain a structure consisting of ferrite and pearlite. Ferrite to austenite transformation took place when the specimens were reheated to 1003–1073 K and held. During the reverse transformation from ferrite to austenite, the pearlitic structure transforms at first to austenite. The concentrations of manganese in austenite and ferrite are almost the same because the austenite to ferrite transformation in the initial structure occurs by the paraequilibrium mode. The initial growth of austenite into ferrite in the intercritical annealing range occurs by diffusion of carbon in austenite and across the interface between austenite and ferrite. This constitutes the second stage of the ferrite to austenite transformation. However, in low carbon steels such as HSLA steels, the relative amount of pearlite is small and the extent of the second stage of ferrite to austenite transformation

is limited. As soon as the diffusion field of carbon in austenite reaches the original grain boundary position, further transformation of ferrite to austenite can occur only under a truncated diffusion field. The situation is ideal for further growth of austenite to occur by the diffusion of manganese in ferrite. This is because the diffusivity of manganese in ferrite is two or three orders of magnitude higher than that in austenite. The growth of austenite by the diffusion of manganese in ferrite constitutes the third stage of the transformation, observed as the formation of Widmanstätten austenite.

The first step is to determine the necessary parameters involved in the calculation, which include supersaturation degree, critical nucleus size, interfacial free energy, diffusion coefficient and the experimental values of the radius of the advancing tip. The equilibrium concentrations of manganese in ferrite and austenite in the Nb-steel as functions of temperature are shown in Fig. 2.2. The temperature for ferrite to disappear in the Nb-steel is 1084 K. This section concentrates on the temperature range below this temperature, where precipitate grows into needles. Temperature increase affects the degree of supersaturation Ω_0 and the size of critical radius. Ω_0 and ρ_c' as functions of temperature are shown in Figs. 2.3 and 2.4.

The molar volume of the austenite phase is $7.304 \times 10^{-6} \text{ m}^3/\text{mol}$, calculated using the weighted average of the molar volumes of pure iron and manganese

Fig. 2.2 Concentration of manganese in ferrite and austenite as functions of temperature in the Nb-steel (From Guo and Sha (2004) © Carl Hanser Verlag, Muenchen)

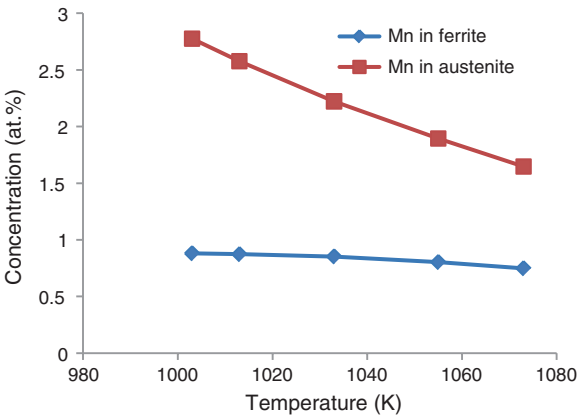
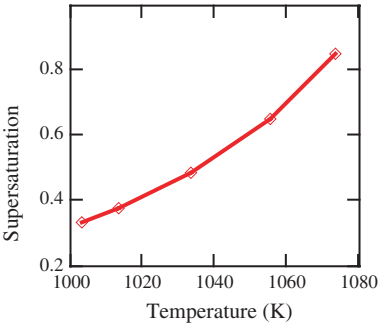


Fig. 2.3 Degree of supersaturation as a function of temperature in the Nb-steel (From Guo and Sha (2004) © Carl Hanser Verlag, Muenchen)



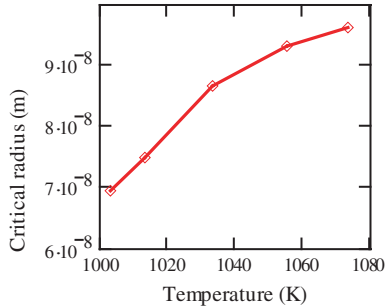


Fig. 2.4 Critical radius size as a function of temperature in the Nb-steel (From Guo and Sha (2004) © Carl Hanser Verlag, Muenchen)

considering Fe-1.5 wt% Mn alloy. The interphase energy of the interface between austenite and ferrite is taken as the value for the interface between α -Fe and γ -Fe, 560 mJ/m², at the advancing tip. The diffusion coefficient of alloying elements in the ferrite matrix is $D = D_0 \exp(-Q/RT)$, where D_0 is the pre-exponential term in Arrhenius expression for the diffusion coefficient and Q is the diffusion activation energy. Parameters are $D_0 = 1.49 \times 10^{-4}$ m²/s and $Q = 233.25$ kJ/mol for ferromagnetic iron in the temperature range 973–1033 K. Between 1073–1173 K, the values for D in paramagnetic iron are used, $D_0 = 3.5 \times 10^{-4}$ m²/s and $Q = 219.45$ kJ/mol. Since the difference in diffusivity values calculated from the two sets of D_0 and Q is small for temperature 1033–1073 K, the ferromagnetic D values are used in this temperature interval.

The values of Peclet number p and ρ/ρ_c' ratio at different degrees of supersaturation from the original theory can be obtained from the work by Rivera-Díaz-del-Castillo and Bhadeshia (2001). The experimental ρ values are used. The experimental values of ρ and calculated ρ/ρ_c' ratios are listed in Table 2.1. At the two temperature points where the experimentally observed radius of the advancing tip for either needle or plate (in this case needle) ρ_e is not known, ρ_e/ρ_c' is interpolated by assuming that there is a linear relationship between ρ_e/ρ_c' and Ω_0 . The ratio between calculated ρ and ρ_e as a function of Ω_0 is shown in Fig. 2.5. The calculated lengthening rates of the Nb-steel using calculated ρ and ρ_e are shown

Table 2.1 Comparison between the calculated ρ/ρ_c' and experimental values for the Nb-steel

Temperature (K)	ρ_c' (nm)	ρ_e (nm)	ρ_e/ρ_c'	ρ/ρ_c' (calculated)	ρ (calculated, nm)	ρ (calculated)/ ρ_e
1003	69	111.2	1.61	6.0	414	3.7
1013	75	-	1.64 ^a	5.7	428	3.5
1033	87	-	1.71 ^a	4.9	426	2.9
1055	93	169.0	1.81	3.9	363	2.2
1073	96	184.4	1.92	2.9	278	1.5

^aEstimated based on the values at 1003, 1055 and 1073 K, by assuming a linear relationship between ρ_e/ρ_c' and the supersaturation degree Ω_0

Fig. 2.5 Ratio between calculated ρ and ρ_e as a function of supersaturation degree for the Nb-steel (From Guo and Sha (2004) © Carl Hanser Verlag, Muenchen)

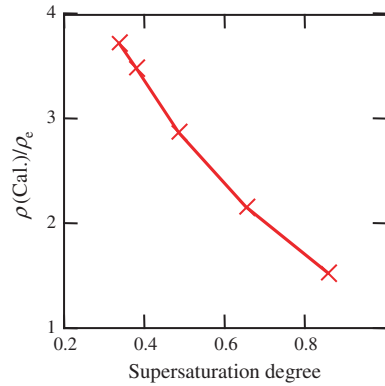
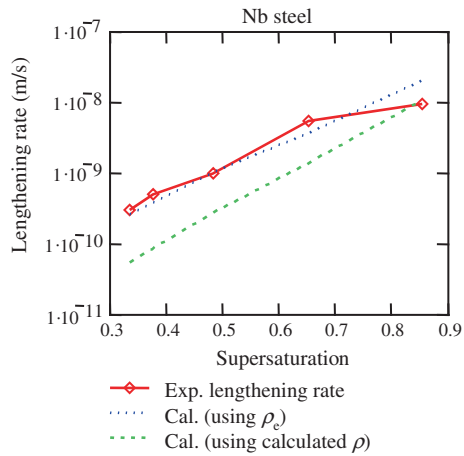


Fig. 2.6 Comparison between experimental and calculated results using calculated ρ and ρ_e , for the lengthening of austenite in the Nb-steel (From Guo and Sha (2004) © Carl Hanser Verlag, Muenchen)



in Fig. 2.6, together with experimental data for comparison. It can be seen that the values using ρ_e fit the experimental data much better than the values calculated using calculated ρ .

The development of the original theory neglects the transformation stress and strain and the anisotropic nature of interphase energy. Consequently, the shape of the precipitate may not be accurately predicted. In order to obtain lengthening rates in agreement with experimental observations, previous studies on precipitate lengthening usually included optimisation procedures on such as interphase energy, interface kinetic coefficients or diffusion coefficient.

The effects of stress and strain caused by precipitate formation and anisotropic interphase energy are reflected in the aspect ratio of the newly formed phase, which can be in turn reflected in the change of the ρ/ρ_c or ρ/ρ_c' ratio. Such effects can be compensated by using the original theory with experimental values of the radius of the advancing tip. The ratio between the theoretically calculated ρ/ρ_c or ρ/ρ_c' with experimental values ρ_e/ρ_c or ρ_e/ρ_c' reflects the compression effects on precipitate morphology due to transformation stress and strain and anisotropic interphase energy.

The focal distance of the advancing tip changes to $\rho_e/\rho(\text{calculated})$ of the value obtained from the original calculation, as illustrated in Fig. 2.7. The relationships between Ω_0 and the Peclet number p are not affected by such revisions. The ρ/ρ_c and ρ/ρ_c' values are calculated using Eqs. 2.7b and 2.6b, respectively. The lengthening rate will be $\rho(\text{calculated})/\rho_e$ times faster if one uses $p = V\rho_e/2D$ in place of $p = V\rho(\text{calculated})/2D$. For instance, the growth rate for precipitate plates will be

$$V = \frac{9}{8\pi} \frac{D}{\rho_e} \Omega_*^2 \quad (2.10)$$

That the original theory is not able to predict the ρ/ρ_c' ratio well is not new. In relation to the growth of Widmanstätten needles in Fe–Mn–C steels, the experimentally observed ρ/ρ_c' ratios for needle growth are about 1.6–1.9. The calculated results using the original model, Eq. 2.5, range from 2.9 to 6, giving $\rho(\text{calculated})/\rho_e$ of 1.5–3.7 (Table 2.1). When studying the lengthening kinetics of ferrite and bainite side plates in Fe–C steels (C from 0.24 to 0.45 wt%), the theoretically calculated radius of curvature is larger than observed experimentally. Ascribing different values to interface kinetics coefficient μ_0 could achieve fair agreement between calculation and experimental observation.

The development of the original theory ignores the existence of transformation stress and strain and the anisotropic nature of interphase energy. Consequently, the calculated radius of the advancing tip (Fig. 1.1) is larger than its real size and the precipitate has a different shape. When quantification of precipitate lengthening using the original theory includes optimisation procedures, errors that are caused by using the wrong calculated tip radius would be transferred to other parameters to be optimised. The geometry of the precipitate will be incorrect, as shown in Fig. 2.7. Using the original theory with experimental values of the radius of the advancing tip compensates the neglected effects from transformation stress and strain and interphase energy on precipitate morphology. It makes the original theory physically more accurate. Purely from a theoretical point of view, when

Fig. 2.7 Illustration of the compression effect on precipitate morphology and tip radius with $\rho(\text{calculated})/\rho_e$. The precipitate geometry from using $\rho(\text{calculated})$ shown here is what one should expect when optimisation procedures were applied to meet the experimental lengthening rate (From Guo and Sha (2004) © Carl Hanser Verlag, Muenchen)

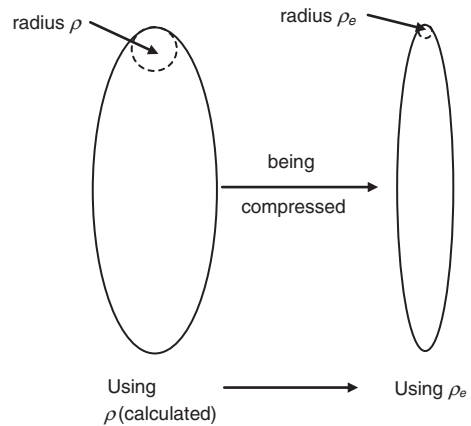


plate growth at small degrees of supersaturation is quantified using the original theory with calculated ρ , the ρ/ρ_c ratio calculated from Eq. 2.7b approaches infinity, when virtually there is no lengthening, Eq. 2.7a. The geometric requirement of the original theory no longer exists. The use of experimental values of the radius of the advancing tip is however of rather phenomenological or empirical nature.

Theoretical determination of the effects from transformation stress and strain and interphase energy remains difficult, which is justified and reflected by the difficulties in theoretical estimation of the aspect ratio of precipitates. Figure 2.5 shows that the value of $\rho(\text{calculated})/\rho_e$ decreases with increasing degree of supersaturation. In fact, the product of $\rho(\text{calculated})/\rho_e \cdot \Omega_0$ is between 1.25 and 1.40 (1.33 ± 0.07), close to a constant, i.e. $\rho(\text{calculated})/\rho_e$ seems to be inversely proportional to the supersaturation degree. If the tip radius of the precipitate is measured at one temperature, $\rho(\text{calculated})/\rho_e$ and the supersaturation degree at that temperature can be calculated. Given another temperature, $\rho(\text{calculated})/\rho_e$ can be estimated since the supersaturation degree is known. The lengthening rate of precipitates at that temperature can therefore be calculated.

As aforementioned, two factors that influence the aspect ratio are transformation stress and strain and the anisotropy of interphase energy. Usually, one or the other dominates the precipitate growth process. When a precipitate is first formed, it is coherent with the matrix. The contribution from the transformation stress and strain is little due to the small size (volume). Interphase energy is the dominant factor. When the precipitate grows into larger size whereas the interface remains coherent, the interphase energy of the coherent interface is small while compared with the strain energy and therefore it can be neglected. When the precipitate grows to a certain size, it will lose coherency with the matrix through the introduction of dislocations into the interface. The energy of the incoherent interface becomes the dominant factor, whose value is much larger than the value of a coherent interface. At a certain stage, it is possible that the compression effect on the advancing tip radius is mainly due to one factor, either transformation strain/stress or the anisotropy of interphase energy.

2.1.3 Summary

A growth theory of precipitates of needle and plate shapes is used in a revised form. The experimental values of the radius of the advancing tip are used to compensate the influences from transformation stress and strain and anisotropic interphase energy on the precipitate morphology, which are ignored in the initial development of the theory. The theory, with the adaptation, is applied to the growth kinetics of Widmanstätten austenite in ferrite in HSLA Fe–C–Mn–Nb steel. Results agree well with the experimental observations. The ratio between theoretical and experimental values of the radius of the advancing tip for the needlelike precipitate growth is inversely proportional to the degree of supersaturation.

2.2 Determination of Activation Energy of Recrystallisation Using a Kissinger Method

Recrystallisation is commonly studied under continuous heating conditions, using differential thermal analysis or differential scanning calorimetry, to measure the heat evolution during the process, and thermal and mechanical simulation, to measure the dimension change during the process. Experiments can be conducted under different heating rates, with higher heating rates increasing the recrystallisation temperature, as it is a thermally activated process. A modified Kissinger method has been developed to evaluate the activation energy of such processes, based on the following equation:

$$\ln \frac{T_f^2}{Q} = \frac{E}{RT_f} + \ln \frac{E}{RK_0} + \ln \beta_f^* \quad (2.11)$$

where T_f is the characteristic temperature for the given process corresponding to a fixed stage of recrystallisation measured for a number of heating rates, Q is the heating rate, E is the activation energy, R is the gas constant and K_0 and β_f^* are constants (Sha 2001). The term T_f can be recrystallisation start, 50 %, or finish temperature. The original Kissinger analysis and variants thereof for determination of activation energies have been derived on the basis of homogeneous reaction kinetics.

Recrystallisation in steels is a process extensively studied in the past and present. The processes under continuous heating have been studied by many workers, using mainly thermal analysis. In this section, the activation energy of recrystallisation in low and ultralow carbon steels (Muljono et al. 2001) is shown.

The heating rates used are 50, 200, 500 and 1000 °C/s. The intention of the original work was to understand the effect of high heating rates on recrystallisation behaviour of cold-rolled steel strip. The transverse flux induction heating may offer advantages over the more conventional annealing processes by reducing annealing time, allowing a more compact annealing line and providing greater control of microstructure and properties. This process is capable of continuously annealing steel strip at heating rates up to 1000 °C/s. The curves of $\ln(T_f^2/Q)$ versus $1/RT_f$ are shown in Figs. 2.8 and 2.9, and the activation energy values calculated from the linear regression shown in the figures are given in Table 2.2. The ultralow carbon steel has higher recrystallisation activation energy compared to the two low-carbon steels. The role of carbon on the activation energy is complicated. The lowest carbon steel (0.003C) has a larger initial grain size, resulting in a small number of nucleation sites. The high recrystallisation activation energy also explains why this steel has much higher recrystallisation temperatures compared to the other two steels.

In Fig. 2.9, the activation energies for recrystallisation in the 0.05C steel after different heat treatments are evaluated in comparison. The hot-rolled sample is the same sample used in Fig. 2.8, but the data were taken from a different diagram

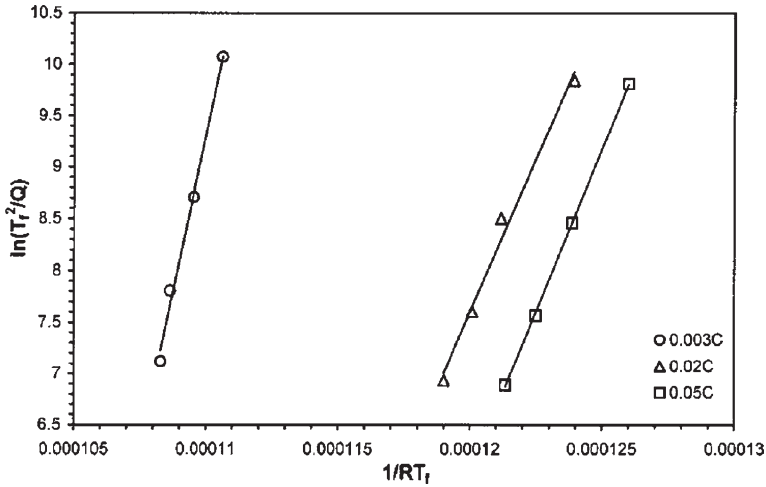


Fig. 2.8 $\ln(T_f^2/Q)$ versus $1/RT_f$ plots for recrystallisation in hot-rolled low and ultralow carbon steels. With kind permission from Springer Science + Business Media: Metallurgical and Materials Transactions A, Determination of activation energy of phase transformation and recrystallization using a modified Kissinger method, 32, 2001, 2903–2904, W. Sha, Fig. 2

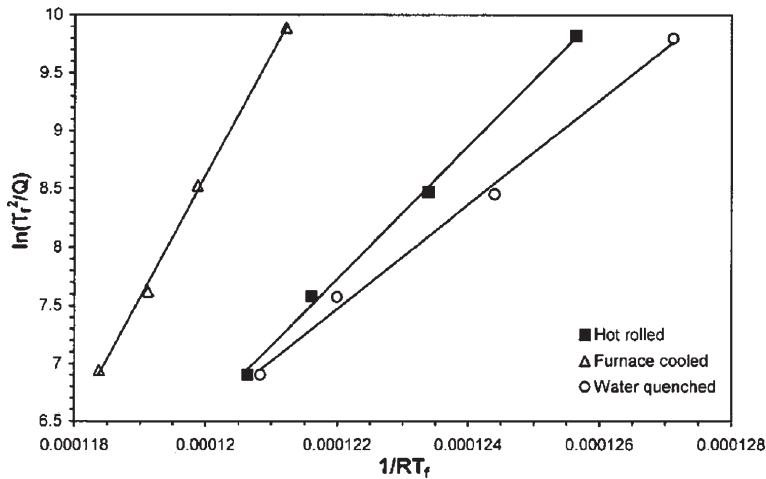


Fig. 2.9 $\ln(T_f^2/Q)$ versus $1/RT_f$ plots for recrystallisation in 0.05C steel after different treatments. With kind permission from Springer Science + Business Media: Metallurgical and Materials Transactions A, Determination of activation energy of phase transformation and recrystallization using a modified Kissinger method, 32, 2001, 2903–2904, W. Sha, Fig. 3

from Muljono et al. (2001), so the difference in the calculated activation energy values gives a measure of the error in the data read from the diagrams in Muljono et al. (2001). This is found to be 59 kJ/mol and is larger than the errors estimated using standard statistical theory for linear regression, for the 0.02 and 0.05C steels under all conditions. Therefore, this is taken as the error of the activation energy

Table 2.2 Recrystallisation activation energy

Steel	Condition	Activation energy (kJ/mol) ^a
0.003C	Hot rolled	1217
0.02C	Hot rolled	591
0.05C	Hot rolled	631
0.05C	Hot rolled	572
	Furnace cooled	1050
	Water quenched	448

^aThe errors are ± 77 kJ/mol for the 0.003C steel, and ± 59 kJ/mol for the other two steels

values obtained. The furnace-cooled sample has a much larger grain size than the water-quenched sample, which results in the higher recrystallisation temperatures as the driving force is reduced. This is also associated with a much higher activation energy for recrystallisation.

2.3 Change of Tensile Behaviour with Tempering Temperature

2.3.1 Microstructure and Tensile Properties

Lower bainite microstructures with pancake-shaped grains are obtained for the steel of a composition as listed in Table 2.3 with the employed thermomechanical control process (TMCP, Yan et al. 2009) (Fig. 2.10). Each pancake grain is around 30 μm thick, 100 μm wide and several hundred microns long. The bainite ferrite laths are characterised by the carbides distributed along the lath boundaries. It is worth noticing that the laths in each grain mainly show only one direction. With increase in tempering temperature, the appearance of ferrite lath boundaries becomes less clear. When the tempering temperature is high up to 700 °C, small recrystallised grains appears, as shown in Fig. 2.10e.

The tensile stress–strain curves (Fig. 2.11) of the steel treated below 400 °C does not show obvious yield phenomenon. However, when the tempering temperature is 500 °C and higher, the upper yield point appears gradually. This phenomenon becomes obvious when the tempering temperature increases from 600 to 650 °C. Another point worth considering is that the tensile curves of the steel tempered at 500–650 °C exhibit plateaus after their yield point. When the tempering temperature is as high as 700 °C, the upper yield point disappears and the tensile curve is characterised by a round roof shape, indicating good formability.

Table 2.3 Chemical composition of the steel (wt%)

C	Mn	Nb	V	Ti	Mo	Cr	Cu	Ni	Si	P	Al	N
0.046	1.79	0.049	0.03	0.023	0.31	0.31	0.2	0.77	0.1	0.0061	0.1	0.003

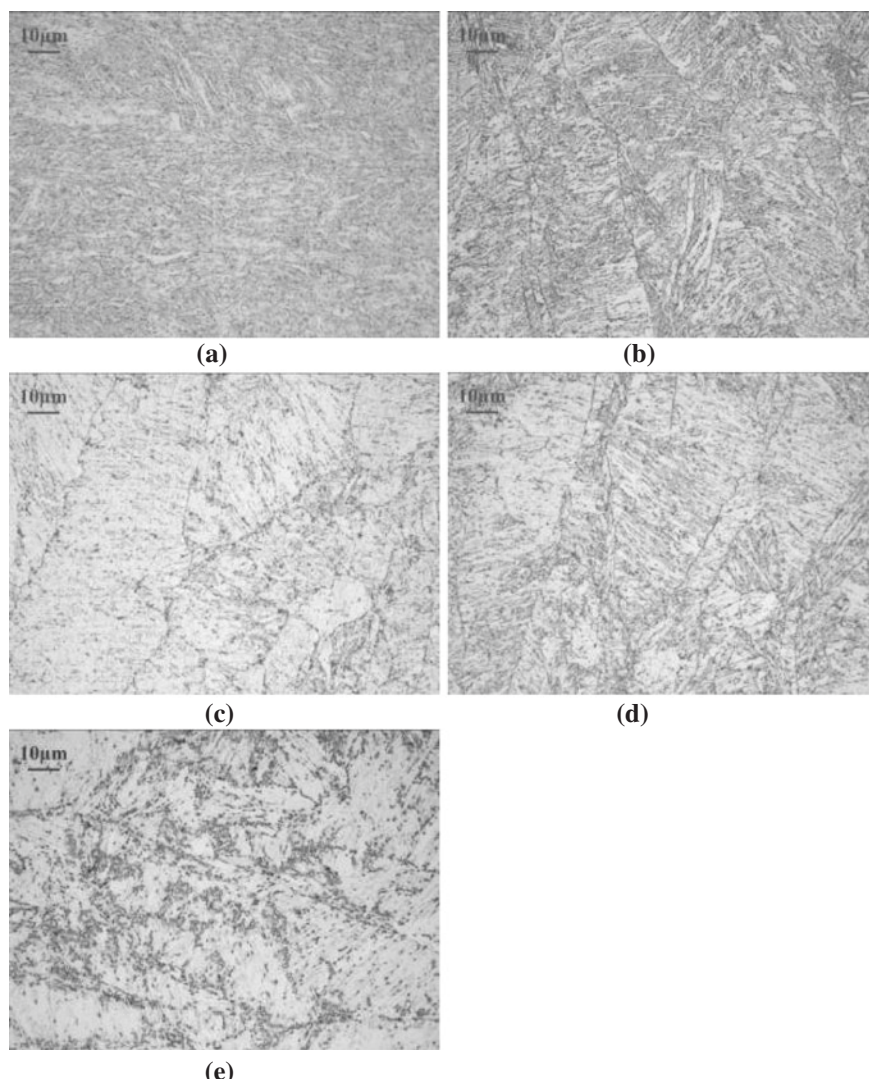


Fig. 2.10 Microstructures of the as-processed steel in the as-rolled and tempered state. **a** As-rolled; **b** tempered at 200 °C; **c** tempered at 400 °C; **d** tempered at 600 °C; **e** tempered at 700 °C. Reprinted from *Materials Science and Engineering: A*, Vol 517, Wei Yan, Lin Zhu, Wei Sha, Yi-yin Shan, Ke Yang, Change of tensile behaviour of a high-strength low-alloy steel with tempering temperature, Pages 369–374, 2009, with permission from Elsevier

In order to present the change in strength, both the yield strengths (YS) and ultimate tensile strengths (UTS) of the steel tempered at different temperatures are shown in Fig. 2.12. This reveals that the yield strength does not decrease with increasing tempering temperatures below 650 °C, even possessing

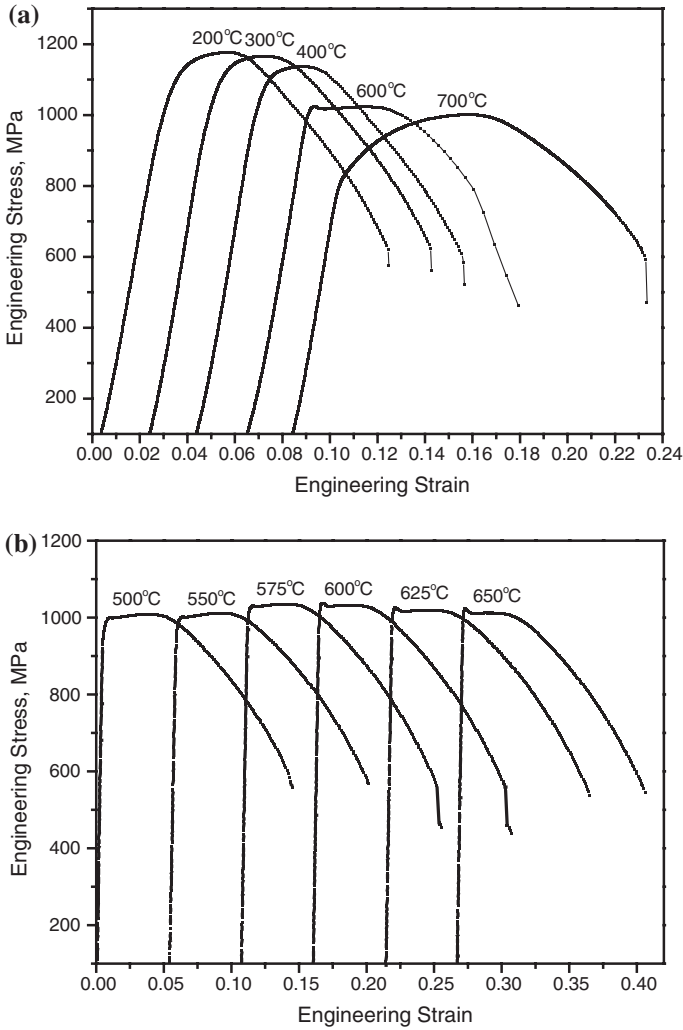


Fig. 2.11 Tensile curves of the steel tempered at different temperature. Reprinted from Materials Science and Engineering: A, Vol 517, Wei Yan, Lin Zhu, Wei Sha, Yi-yin Shan, Ke Yang, Change of tensile behaviour of a high-strength low-alloy steel with tempering temperature, Pages 369–374, 2009, with permission from Elsevier

a small peak at 600 °C. Nevertheless, the tensile strength remarkably decreases to about 1000 MPa when tempered at 500 °C and is close to the yield strength when the tempering temperature is up to 650 °C. At the highest tempering temperature of 700 °C, the yield strength decreases more steeply than the tensile strength. Therefore, with increasing temperature the difference between the tensile strength and the yield strength becomes smaller and smaller, and it almost

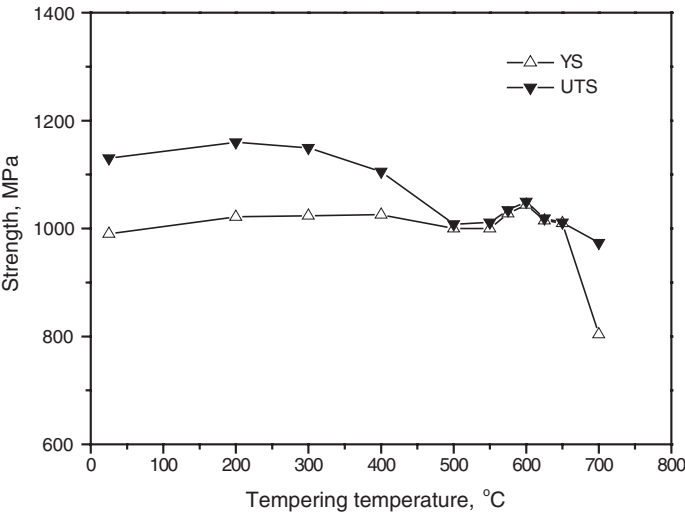


Fig. 2.12 Ultimate tensile strength (UTS) and yield strength (YS) of the HSLA steel as functions of the tempering temperature. Reprinted from Materials Science and Engineering: A, Vol 517, Wei Yan, Lin Zhu, Wei Sha, Yi-yin Shan, Ke Yang, Change of tensile behaviour of a high-strength low-alloy steel with tempering temperature, Pages 369–374, 2009, with permission from Elsevier

Table 2.4 Strain hardening exponent n of the steel tempered at 500–650 °C

Tempering temperature (°C)	strain hardening exponent n
500	0.036
550	0.036
575	0.029
600	0.076
625	0.029
650	0.021

vanishes in the temperature range between 500 and 650 °C. When the tempering temperature reaches 700 °C, the difference in the stress values increases.

The strain hardening exponents for differently heat-treated steel according to Eqs. 1.3–1.5 are given in Table 2.4. The strain hardening exponent decreases slightly when the tempering temperature is below 400 °C, but is subjected to an abrupt decrease to as low as 0.021, when the tempering temperature is 650 °C. At the tempering temperature of 700 °C, the n value increases to 0.258. The strain hardening exponent also displays a peak at the tempering temperature of 600 °C.

2.3.2 The Upper Yield Point

For tempering at 500 °C, dislocations in the steel should have enough thermal energy to move and interact with each other. Thus, many dislocations with

opposite Burgers vectors, i.e. the positive and negative dislocations, would interact and will annihilate. Consequently, the dislocations density will considerably decrease. The ferrite lath boundaries would also begin to disappear due to the movement of dislocations, as shown in Fig. 2.10c. Simultaneously, iron carbide precipitates should form during treatment at this temperature, since the dissolved carbon atoms have been activated, resulting in quite fast diffusion. Then, the precipitates act as strong pinning obstacles for dislocations glide. Therefore, the mobile dislocations density will be strongly reduced. On the other hand, the reduced dislocations density and disappearing lath boundaries in turn afford much space for moving dislocations. A higher stress will be needed in order to drive the dislocations off the pinning to move. Thus, the upper yield strength occurs. When the dislocations break away from the pinning precipitates, the mobile dislocations density will increase again. Hence, the stress needed for gliding dislocations decreases. Consequently, it is reasonable that the upper yield point appears on the stress–strain curves of the steel when the tempering temperature is above 500 °C, according to the above-described mechanisms. With increasing tempering temperature, more ferrite laths disappear and the dislocations density will be reduced, while the amount of precipitation increases. From this, it is deduced that the upper yield point will become more pronounced with increasing tempering temperature. The nucleation temperature for large amount of precipitations in HSLA steels is about 600 °C (Chap. 3), which is related to the upper yield point and the yield strength peak. However, it is noteworthy that there is only one peak in the tensile curves, not like the typical oscillating yield points (Portevin-LeChatelier effect) on stress–strain curves of mild steels, because the mobile dislocations density cannot be reduced effectively in this steel.

However, tempering at 200 °C will lead to the moving dislocations in the steel interacting with point defects such as vacancies and interstitial atoms. The mobile dislocations density may be much lower and will hardly increase. If the tempering temperature increases up to 300 and 400 °C, the dislocations will be able to move and interact with each other, but the density might not be strongly reduced, which indicates the small change in the strength. Additionally, the ferrite lath boundaries are still stable, so the mean free path of gliding dislocations is restricted. Even if they will move, other immobile dislocations and the ferrite lath boundaries would immediately block them. Therefore, the amount of mobile dislocations will hardly increase. Hence, the upper yield points do not appear in the steel tempered at 300 and 400 °C.

When the tempering temperature increases up to 700 °C, recrystallisation occurs. Coarsening of precipitates in the steel takes place and the effective pinning of dislocations diminishes. Therefore, the yield strength of the steel shows a strong decrease. The mobile dislocations density may be quite low and dislocation glide is inhibited by a large number of newly formed grain boundaries in the recrystallised grains. Thus, the density of mobile dislocations cannot significantly increase. Therefore, the upper yield points do not appear on tensile curves.

2.3.3 Strain Hardening Exponent

The strain hardening exponents are calculated for the uniform plastic deformation range. A lower strain hardening exponent indicates that the material possesses a lower strain hardening ability. Generally, the as-recrystallised metals and alloys and the severely strain hardened material show this feature of a low n value. The primary reason in the case of the as-recrystallised metals and alloys is that the matrix has not enough barriers for the moving dislocations, and the reason in the case of the severely strain hardened materials is that the dislocations cannot move any more in the matrix. In either case, the yield strength is nearly equal to the tensile strength, for the described tempered steel at 500–650 °C, as shown in Fig. 2.12.

The phenomenon of low strain hardening exponents of HSLA steels is unexpected. The steel tempered at 500–650 °C is obviously not so strongly strain hardened, as described as the second reason above. No recrystallisation occurs at these temperatures; see the primary reason as aforementioned. Therefore, there must be a third reason. Lowering of n value for continuously annealed cold-rolled steel has been observed because of boron additions (Funakawa et al. 2001). The n value decreases significantly when the carbon content in steel is lower than 0.002 %. The reason for this is explained in terms of morphological changes of the carbide precipitates in matrix and at grain boundaries. Antoine et al. (2005) analysed the relationship between n and the yield strength of titanium containing IF steel. The n value is controlled by dislocation-precipitate and dislocation-grain boundary interactions. Smaller amount of dissolved carbon and nitrogen atoms reduces the efficiency of grain boundaries to block the dislocations movement and thus a decrease in the n value. Therefore, tempering at 500–650 °C can result in a depletion of the dissolved carbon and nitrogen atoms due to the precipitation of ϵ -carbides (FeC_2) or carbonitrides, which might be responsible for the low strain hardening exponent. In addition, the decrease in the dislocation density as well as the disappearing of the ferrite lath during tempering would contribute to the low n value.

The precipitates could also pin gliding dislocations, and hence increase the strain hardening rate. From the above-described results, it is concluded that the dissolved carbon and nitrogen atoms and their interactions with dislocations have a much stronger effect on the strain hardening exponent than the precipitates. The n value will increase gradually with an increase in the amount of precipitates, but n decreases steeply with the decrease in the content of dissolved carbon and nitrogen atoms. The formation of the precipitates would consume the dissolved carbon and nitrogen atoms, which can be demonstrated from the relation between the strain hardening exponent and the content of the dissolved carbon and nitrogen atoms as shown in Fig. 2.13. The increasing amount of precipitates is consistent with the decreasing content of dissolved carbon and nitrogen atoms. Therefore, the n value shows a considerable change as illustrated by the bold line in Fig. 2.13, i.e. the n value reaches a minimum at 575 °C. When the tempering temperature is above 600 °C and increases up to 650 °C, the precipitation kinetics is saturated

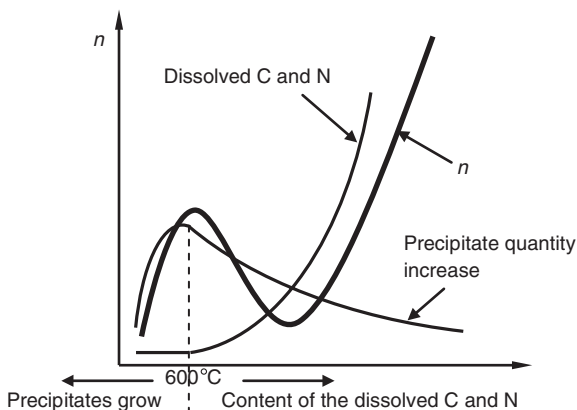


Fig. 2.13 Schematic representation of the strain hardening exponent variation as a function of the dissolved carbon and nitrogen atoms contents and the quantity and size of the precipitates. Reprinted from Materials Science and Engineering: A, Vol 517, Wei Yan, Lin Zhu, Wei Sha, Yi-yin Shan, Ke Yang, Change of tensile behaviour of a high-strength low-alloy steel with tempering temperature, Pages 369–374, 2009, with permission from Elsevier

and the growth rate of the precipitates decreases. Hence, the n value decreases again. Therefore, the n value shows a small peak at 600 °C since the 600 °C tempering can produce the largest number of fine precipitates. This explanation agrees well with the results shown in Table 2.4 and Fig. 2.12.

When tempering at 700 °C, the newly formed, small, recrystallised grains not only increase the amount of grain boundaries, but also behave as the second phase, resulting in high strain hardening ability of this steel.

2.3.4 Summary

Lower bainite microstructure causing high strength of the HSLA steel is achieved by proper thermomechanical control process. The yield strength of the steel shows a slight increase up to the tempering temperature of 550 °C, then passing a maximum at 600 °C. Beyond 650 °C, the yield strength decreases steeply. The tensile strength decreases beyond 200 °C and becomes close to the yield strength when the tempering temperature ranges between 500 and 650 °C.

There is no pronounced yielding point appearing on the tensile curves of the steel tempered below 400 °C. However, the steel gradually develops upper yield points with relatively low strain hardening exponents when the tempering temperature is increased from 500 to 650 °C. The low strain hardening exponent reaches a peak at 600 °C. This can be explained in view of the interactions of the mobile dislocations with the dissolved carbon and nitrogen atoms and their effect on the strain hardening exponent.

The steel tempered at 700 °C shows ‘round roof’ shaped tensile curves possessing high strain hardening exponents due to the fine-grained microstructure in the as-recrystallised state. The governing mechanism is the strong interactions of dislocations and interstitials with grain boundaries and the fine-dispersed precipitates of carbides and carbonitrides.

2.4 Delamination Fracture Related to Tempering

2.4.1 Microstructures

The as-rolled steel (composition in Table 2.3) has a lower bainite microstructure. The microstructure of a transverse section is shown in Sect. 2.3. The microstructures of the tempered steel in the longitudinal or rolling direction are shown in Fig. 2.14. The length of the pancake grains along the rolling direction is much larger than the width, which is an obvious characteristic of the anisotropic microstructure. Before rolling, the grains are equiaxed and the size is 50–100 μm when soaked at 1200 °C. After rolling at austenite recrystallisation zone, the grain size could be refined to 20 μm . With increase of the tempering temperature, the ferrite laths in the grains disappear and the prior austenite grain boundaries become more evident, which should indicate a change in the matrix precipitates. There is little change after tempering at 200–600 °C. During tempering at 700 °C, reaustenitisation begins, so many small ferrite grains are observed in the microstructure.

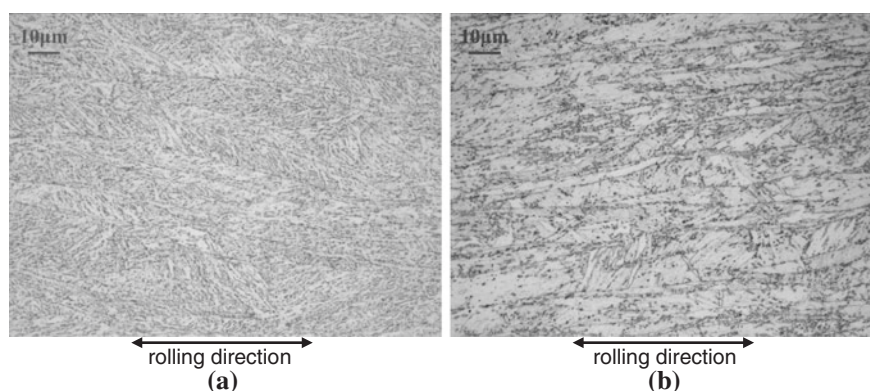


Fig. 2.14 Optical micrographs showing the microstructures of the as-rolled and of the tempered steel along the rolling direction (longitudinal sections). **a** As-rolled; **b** tempered at 700 °C. The etchant was 4 % nital. With kind permission from Springer Science + Business Media: Metallurgical and Materials Transactions A, Delamination fracture related to tempering in a high-strength low-alloy steel, 41, 2010, 159–171, Wei Yan, Wei Sha, Lin Zhu, Wei Wang, Yi-Yin Shan, Ke Yang, Fig. 3

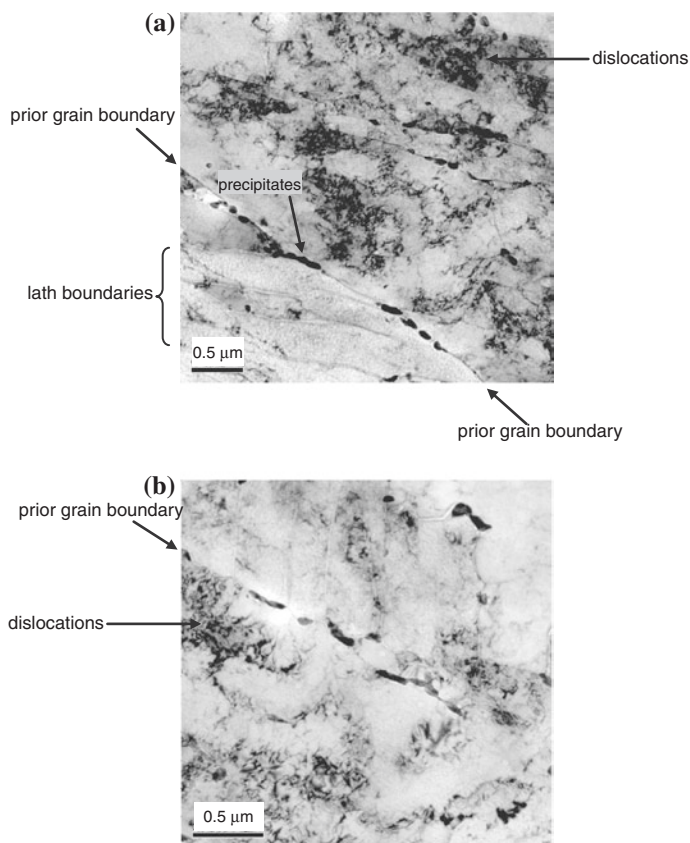


Fig. 2.15 TEM micrographs showing precipitates, probably alloy carbonitrides, in the boundaries of the elongated grains in the steel tempered at 600 °C. With kind permission from Springer Science + Business Media: Metallurgical and Materials Transactions A, Delamination fracture related to tempering in a high-strength low-alloy steel, 41, 2010, 159–171, Wei Yan, Wei Sha, Lin Zhu, Wei Wang, Yi-Yin Shan, Ke Yang, Fig. 4

Figure 2.15 shows two TEM images of material tempered at 600 °C. Precipitates, most likely carbides and nitrides, are densely distributed along the boundaries of the elongated grains in this steel, proving that tempering at 600 °C leads to grain boundary precipitation. The dense dislocations are a result of the heavy deformation during rolling. The mottled structure inside the grains in the TEM micrographs may be due to surface oxidation of the TEM thin foil between the times when the specimen was made and the microscopy imaging. Such contrast, however, does not interfere with the microstructural features being discussed here, viz. precipitates and grain boundaries. Mottled contrast also arises in some optical and scanning electron microscopy images, for similar reasons and possible surface contamination and inhomogeneous etching.

The precipitates seen in optical micrographs are not the same precipitates observed in TEM, as the magnifications are at very different levels. The precipitates

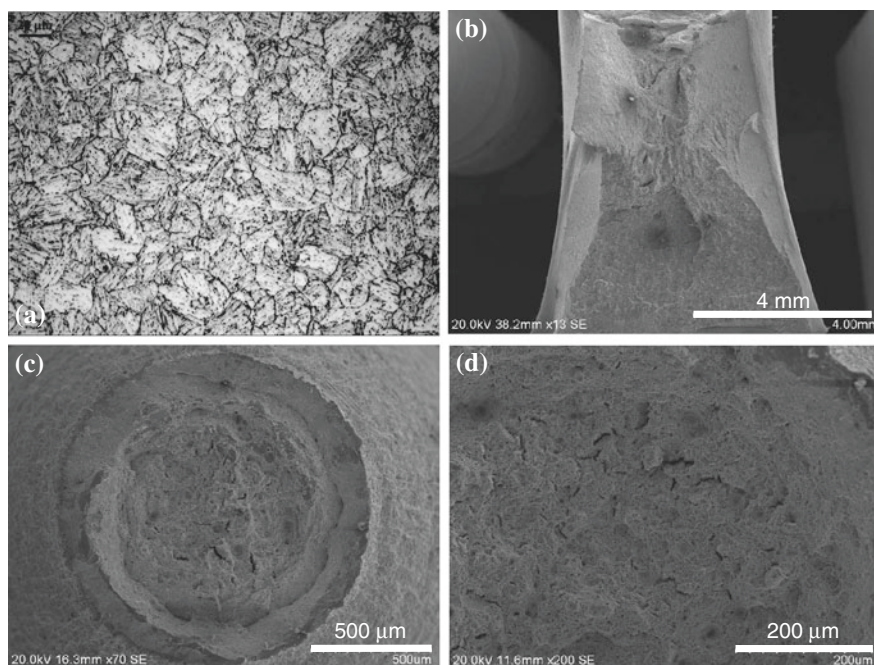


Fig. 2.16 Optical photomicrograph and SEM fractographs of the triple quenched and tempered, equiaxed grain steel. **a** Optical image showing equiaxed grains; **b** fractograph of a sample after impact at $-30\text{ }^{\circ}\text{C}$; **c** fractograph of the room temperature tensile sample; **d** magnified from **(c)** showing small cracks. With kind permission from Springer Science + Business Media: Metallurgical and Materials Transactions A, Delamination fracture related to tempering in a high-strength low-alloy steel, 41, 2010, 159–171, Wei Yan, Wei Sha, Lin Zhu, Wei Wang, Yi-Yin Shan, Ke Yang, Fig. 5

apparent in optical micrographs such as those in Figs. 2.14 and 2.16a are much larger precipitates, which may be inclusions, made to appear bigger due to the etching effect. Their number density is actually very low, orders of magnitude lower than the type of precipitates in the TEM scale. The precipitates in the optical scale, though apparently evenly distributed throughout the entire microstructure, are not relevant to the discussion in this section, because of their very small numbers (though appearing numerous on the optical micrographs due to their low magnification).

After triple quenching and tempering heat treatment, small equiaxed grains of around $25\text{ }\mu\text{m}$ form in the steel (Fig. 2.16a). There are precipitates distributed along the grain boundaries that accentuated the outline of the grains.

2.4.2 Delamination on Tensile and Impact Fracture Surfaces

The steel tempered at 200, 400 and $700\text{ }^{\circ}\text{C}$ shows no delamination on tensile fracture surfaces, while remarkable delamination occurs on the fracture surfaces of the tensile specimens tempered in the range of $500\text{--}650\text{ }^{\circ}\text{C}$ (Yan et al. 2010).

The tensile fracture surfaces with delamination no longer display typical cup-and-cone fracture. This may indicate poor ductility. The fracture surfaces are separated into two halves approximately in the middle of the fracture, which would correspond to the mid-thickness of the rolled plate. Many local undeveloped splits lay on the surface, parallel to the main one. Although there is no delamination in the fracture surfaces of the steel tempered at 200, 400 and 700 °C, small split-like cracks are distributed along the same direction. This type of small cracks is also in the fracture surface of the steel tempered at 500 °C, parallel to the main split.

The details of delamination on each impact fracture surfaces at −30 °C are summarised in Table 2.5. The impact fracture surfaces at room temperature have no delamination, with impact energy 50 J for as-rolled steel, and 48 J for the steel tempered at 500, 600, and 650 °C. The −30 °C impact fracture surfaces of the steel tempered at different temperatures are shown in Fig. 2.17. With increase of the tempering temperature, delamination in these fracture surfaces first increases in both number and length, and then decreases in both. A quantitative measure of degree of splitting could be made by measuring the total length of split per unit area of fracture surface. Multiple continuous splitting occurs in the fracture surface of the steel tempered in the range of 500–650 °C, while single local splitting is in the top (near the notch) area of the fracture surfaces of the steel tempered at 400 and 700 °C and no splitting is on the fracture surface of the steel tempered at 200 °C. Continuous splitting does not extend all the way to the back of the fracture surface when the tempering temperature is 650 °C, and is limited to the area near the notch when the tempering temperature reaches 700 °C.

The continuous, deep splitting segments the delaminated fracture surface, with what appears to be 45° shear fracture between the splits. Small local splits are in the fracture surfaces, as well as large delamination. The details of the surfaces are displayed in Fig. 2.18. Smooth fracture surfaces mixed with ductile fracture areas are illustrated. The smooth fracture surface likely indicates grain boundary decohesion, as can be clearly seen in Fig. 2.18c marked with a black arrow. Song et al. (2006) explain this phenomenon in more detail.

Table 2.5 Impact toughness and fracture splitting of the tempered steel at −30 °C on half-size specimens (5 mm thick)

Tempering temperature (°C)	Impact energy (J)	Splitting
As-rolled	56	No
200	60	No
300	50	No
400	51	Local
500	47	Throughout
550	45	Throughout
575	49	Throughout
600	50	Throughout
625	53	Throughout
650	49	Throughout
700	55	Local

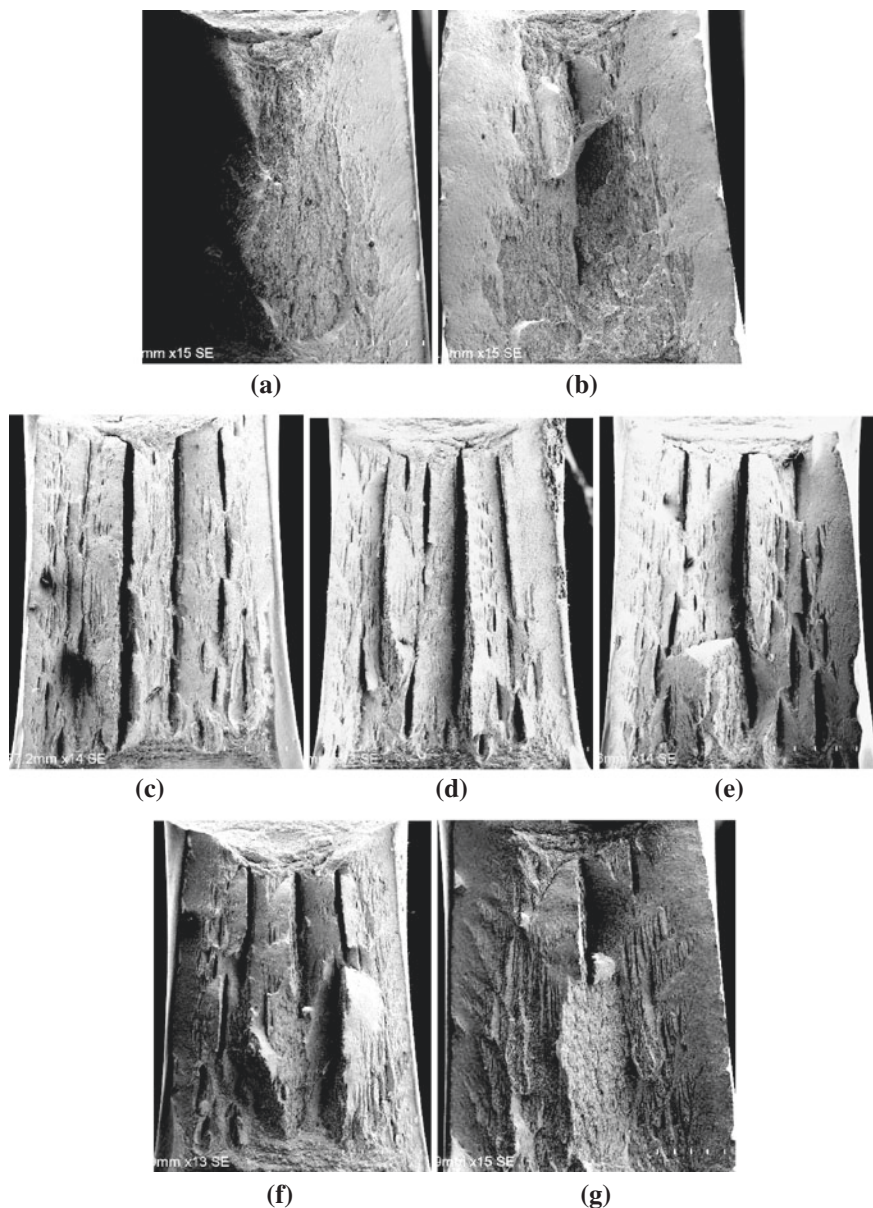


Fig. 2.17 Macrofractographs of the impact fracture surfaces at $-30\text{ }^{\circ}\text{C}$, showing the development of delamination with tempering temperature from none to severe to mild splitting. Tempered at **a** $200\text{ }^{\circ}\text{C}$; **b** $400\text{ }^{\circ}\text{C}$; **c** $500\text{ }^{\circ}\text{C}$; **d** $550\text{ }^{\circ}\text{C}$; **e** $600\text{ }^{\circ}\text{C}$; **f** $650\text{ }^{\circ}\text{C}$; **g** $700\text{ }^{\circ}\text{C}$. The entire width of the impact specimens, 5 mm, is shown in each image. With kind permission from Springer Science + Business Media: Metallurgical and Materials Transactions A, Delamination fracture related to tempering in a high-strength low-alloy steel, 41, 2010, 159–171, Wei Yan, Wei Sha, Lin Zhu, Wei Wang, Yi-Yin Shan, Ke Yang, Fig. 11

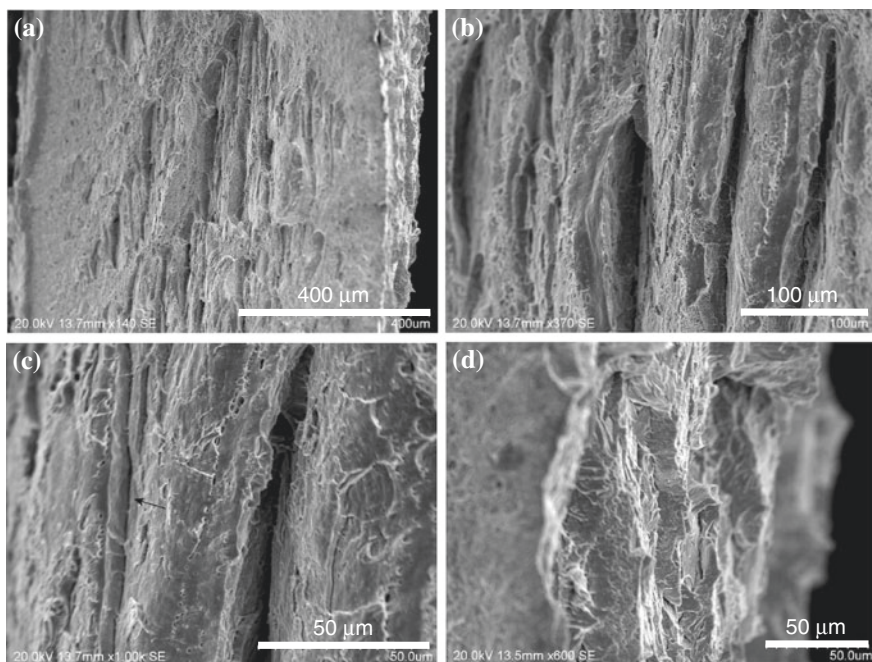


Fig. 2.18 SEM fractographs showing the details of impact fracture surfaces of the steel tempered at 600 °C. **a** Delaminated fracture surface; **b** magnified; **c** magnified from **(b)** showing decohesion; **d** edge of the piece. Since the steps are not in the same plane, the area near the left and right edges of the images is faint. With kind permission from Springer Science + Business Media: Metallurgical and Materials Transactions A, Delamination fracture related to tempering in a high-strength low-alloy steel, 41, 2010, 159–171, Wei Yan, Wei Sha, Lin Zhu, Wei Wang, Yi-Yin Shan, Ke Yang, Fig. 12

2.4.3 Fractography of the Equiaxed Grain Sample and Toughness

When the triple quench heat treatment changes the elongated grains into the equiaxed morphology, delamination disappears from the fracture surfaces after the -30 °C impact and the room temperature tension even after tempering at 600 °C (Fig. 2.16b, c). However, instead of the general delamination seen previously, many small secondary cracks are seen on the tensile fracture surface (Fig. 2.16d).

The Charpy V-notch impact energy is generally employed to characterise the toughness of steel. The toughness values, at -30 °C, of this HSLA steel, with elongated grains, tempered at different temperatures are given in Table 2.5. The steel has a similar level of toughness for all the tempering temperatures. The steel as-rolled and tempered at 200 °C has higher toughness values of 56 and 60 J, respectively, and the other tempering temperatures all lead to toughness around 50 J. When the elongated grains are changed into equiaxed grains, the steel has a little higher toughness of 65 J at -30 °C due to the small grain size.

2.4.4 Splitting Tip Metallography and XRD of the Tempered Steel

The tip of the split in the impact fracture surface from the steel tempered at 500 °C is shown in Fig. 2.19. The crack path is clearly revealed by both optical microscope and SEM to propagate along the prior austenite grain boundaries. The split can make minor adjustments in direction when crossing a grain boundary, as is clearly illustrated by the step-like morphology at the edge of the delaminated pieces shown in Fig. 2.18d. Since the steps are not in the same plane, the ambient area of the image is faint.

X-ray diffraction can qualitatively evaluate the presence of crystallographic texture in steel by the relative heights of the main diffraction peaks. Those planes with peaks showing much stronger intensity than from an entirely random sample would be qualified to be the orientation of texture. The main peaks of the body centred cubic structure show a somewhat higher than expected intensity for the (110) peak relative to the (200) and (211) peaks (Table 2.6), which indicates that some, limited texture may have existed in the tempered samples. The diffraction was from planes parallel to the rolling plane of the steel plate (Yan et al. 2010).

In the above sections, we have examined the phenomenon of delamination or splitting of tensile and impact fracture surfaces of a control-rolled and quenched, HSLA steel when loaded after tempering in the temperature range of 200–700 °C. In Sect. 2.3, the tensile and strain hardening behaviour is discussed. A summary of some of the important observations of Sect. 2.3 is appropriate:

- (1) The microstructure in the as-rolled condition consists of lower bainite (ferrite laths containing elongated cementite precipitates and a high dislocation density) in highly elongated, flat prior austenite grains.
- (2) After tempering at 200–400 °C, the steel exhibits normal stress-strain behaviour, strain hardening exponents of 0.11–0.13, and yield-tensile ratios of approximately 0.85.
- (3) Upon tempering in the range of 500–650 °C, a yield point behaviour is observed, with strain hardening exponents of only 0.02–0.08 (i.e. essentially no strain hardening) and yield-tensile ratios of essentially unity (i.e. the maximum stress occurs at or near yield).
- (4) There is a modest increase in the yield and tensile strengths across this tempering temperature range, with a maximum strength at 600 °C, similar to secondary hardening in the tempering of martensite.

Table 2.6 Relative intensities of the XRD peaks of the steel tempered at different temperatures

Peak index	Standard (no texture)	200 °C	400 °C	600 °C	700 °C
110	100	348	284	262	335
200	20	14	18	13	12
211	30	30	30	30	30

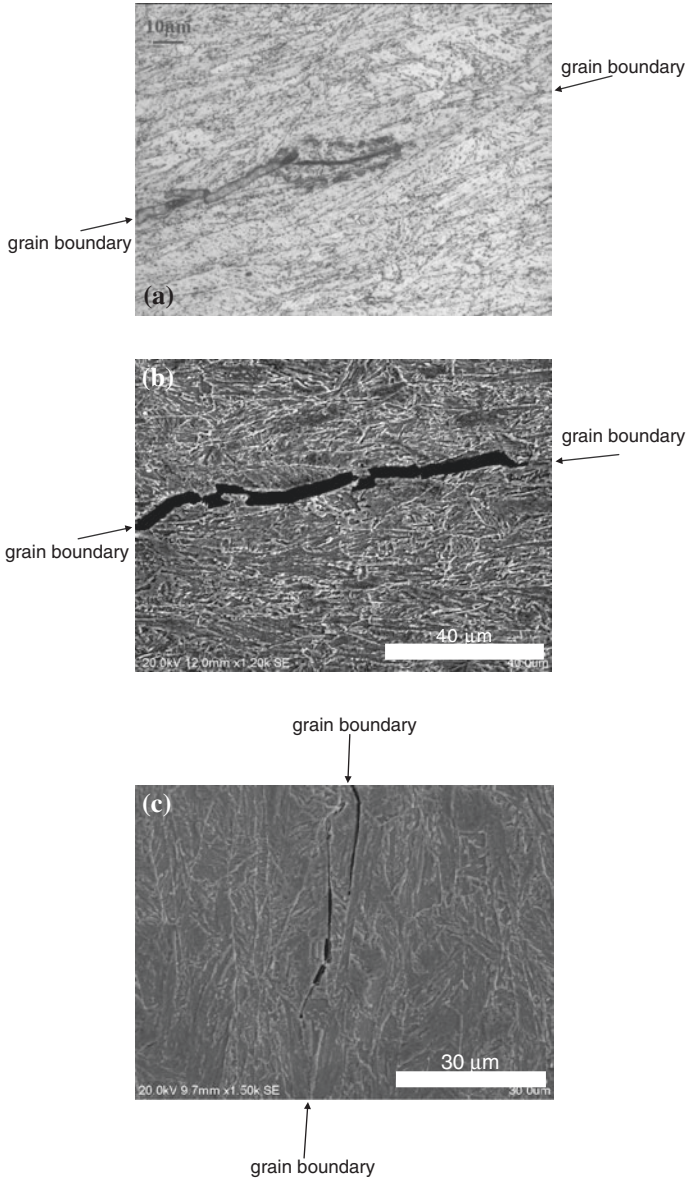


Fig. 2.19 Metallographic section through the tip of a split showing that crack propagation is along the grain boundaries. **a** Optical image showing the splitting tip. The etchant was 4 % nital. **b** SEM image showing the crack propagation path. **c** SEM image showing the splitting tip. With kind permission from Springer Science + Business Media: Metallurgical and Materials Transactions A, Delamination fracture related to tempering in a high-strength low-alloy steel, 41, 2010, 159–171, Wei Yan, Wei Sha, Lin Zhu, Wei Wang, Yi-Yin Shan, Ke Yang, Fig. 13

- (5) Tempering at 700 °C produces a return to normal behaviour, with a strain hardening exponent of 0.25 and a yield-tensile ratio of about 0.8.

The important aspects of the present section (Sect. 2.4) so far that require discussion include:

- (1) The microstructural changes occurring during tempering at temperatures in the range of 500–650 °C cause the steel to be susceptible to delamination during subsequent tensile and impact loading.
- (2) The stress conditions lead to splitting of the room temperature tensile specimens, no splitting of room temperature impact specimens and severe splitting of the –30 °C impact specimens.
- (3) The effect of delamination on the toughness values is obtained.

2.4.5 Delamination and the Anisotropic Microstructure

As mentioned above, delamination behaviour in hot-rolled steels is associated with many different phenomena, all related to anisotropic microstructure. Of those previously identified, the possible anisotropic microstructural features causing delamination could be texture, planar inclusion arrays, aligned precipitates and the elongated grain structure. In the present case, texture can be eliminated for the following reasons. First of all, the steel is not rolled within the two phase alpha-plus-gamma region that has been shown to favour the formation of strong textures (Yang et al. 2008). The strong (100) cleavage plane texture increases with increased annealing temperatures and the textures are retained during annealing up until full recrystallisation (Tsuji et al. 2004). Therefore, if texture played an important role in the observed delamination, the most serious cases should have occurred in the as-rolled or the low temperature tempered specimens, instead of those tempered at 500–650 °C. Furthermore, the XRD shows that there is no significant difference in texture among the tempered steel, confirming the above inference. The (110) peak relative to the (200) and (211) peaks is somewhat high, but (110) is not a normal cleavage plane and there is no trend with tempering temperature.

Precipitation is believed to become predominant when the steel is tempered in the temperature range of 500–650 °C. The precipitates have good opportunity to be one of the reasons for the delamination. With the purpose of distinguishing the roles of elongated grains and precipitates, it is necessary to evaluate the contribution of the elongated grain structure on the delamination. Hence, the as-rolled steel is subjected to the triple oil quench heat treatment that changes the elongated grains into an equiaxed grain structure. The steel, once having equiaxed grains, displays no delamination in the impact fracture surface at –30 °C, even after tempering at 600 °C. This finding indicates that elongated grains are a necessary condition for delamination. The steel even with the highly elongated grain structure shows no extensive delamination as long as the tempering temperature is not in the range of 500–650 °C. In this tempering temperature range, by analogy to martensite tempering, the cementite

precipitates in the bainite most likely go into solution as carbide particles of the strong carbide forming elements in the steel (titanium, niobium, vanadium, molybdenum and chromium) precipitate within the grains and on the grain boundaries.

These two aspects suggest that the elongated grains resulting from hot rolling below the austenite recrystallisation temperature, and the densely aligned precipitates formed during tempering are likely responsible together for the severe delamination. The sole presence of either one would not lead to delamination. This observation also leads to the hypothesis that the precipitates embrittle the grain boundaries and make them the most probable propagation path of delamination. This speculation is actually demonstrated by the investigation of the splitting tip. In Fig. 2.19, the splitting crack propagation path was along the prior austenite grain boundaries. The smooth fracture surfaces on the pieces separated by splitting, in Figs. 2.18a–c, are another proof of the splitting propagation along grain boundary. Thus, it is clear that the continuous splits on the tensile and impact fracture surfaces are in the same direction and parallel to the plane of the flat, elongated grains, as depicted in Fig. 2.20.

The small cracks on the tensile fracture surface of the equiaxed grain steel, as shown in Fig. 2.16d, indicate that the precipitates formed during 600 °C tempering also make the equiaxed grain boundary brittle and easily separated, which further proves the hypothesis. However, due to the grain refinement, the grain boundary area per unit volume is enormously increased, and the precipitates per unit grain-boundary area would have been greatly reduced. Therefore, the embrittlement effect is diminished. Furthermore, the equiaxed grain structure would inhibit crack propagation, while the elongated grains can scarcely change the propagation direction due to their flat, elongated shape. Thus, delamination does not occur due to the absence of its favourable microstructural feature of the elongated grain structure.

Increasing the annealing temperature to beyond the reaustenitisation range, i.e. normalising, can eliminate the splitting phenomenon. Reaustenitisation replaces the anisotropic microstructure with an isotropic one. Therefore, delamination would be difficult and unlikely without such anisotropy. When the steel is tempered at 700 °C, reaustenitisation is not complete. Additionally, reaustenitisation starts primarily along the grain boundaries, which would have depleted the precipitates and erased the embrittlement effect. Hence, although significantly decreased, splitting is not eliminated.

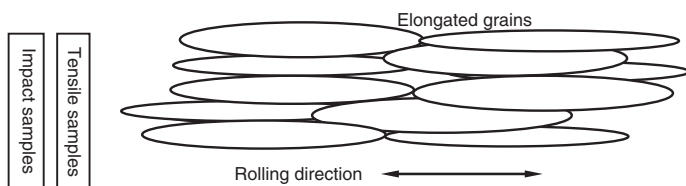


Fig. 2.20 Schematic plan view diagram of the rolled plate showing elongated grain structure and orientation of the tensile and impact test specimens. With kind permission from Springer Science + Business Media: Metallurgical and Materials Transactions A, Delamination fracture related to tempering in a high-strength low-alloy steel, 41, 2010, 159–171, Wei Yan, Wei Sha, Lin Zhu, Wei Wang, Yi-Yin Shan, Ke Yang, Fig. 1

2.4.6 Delamination and the Stress Conditions, and Effect of Delamination on Toughness

An anisotropic microstructure alone cannot lead to delamination; the stress conditions are a second important and, in fact, necessary factor. These stress conditions are actually dependent on the mechanical properties, especially the ductility, of the materials and the geometric dimension, especially the thickness, of the specimens. In both a Charpy impact test and a tensile test, a state of plane strain (i.e., a triaxial tensile stress) emerges. The deformation under plane strain conditions is so highly constrained that the stresses in this rigid zone can reach two to three times the yield stress (Yan et al. 2007).

This rigid plane strain zone is located in the centre of the neck in a cylindrical tensile specimen. The stress state in the neck of a tensile specimen consists of a uniform axial stress plus a hydrostatic tensile component. The hydrostatic component varies from zero at the neck surface to a maximum at the centre line, with the magnitude dependent on the degree of necking and the neck profile. Therefore, delamination in a tensile specimen can be fully developed in the middle, separating the fracture surface into half, provided there exists a plane of weakness. Necking generally begins and uniform strain ends at the maximum load or engineering stress. The split-like cracks in Yan et al. (2010) are undeveloped because of lack of the sufficiently strong stress condition due to the considerable uniform ductility of the steel. It is worth noting that the room temperature tensile specimens tempered at 500–650 °C all display the delamination phenomenon. The specimens should have experienced a certain amount of uniform plastic deformation before necking since the loading speed is low in tensile test. However, in the tensile tests, following tempering in the critical range, the maximum engineering stress occurs at or very near yield, so necking is premature and intense. Therefore, the radial and tangential stresses acting on the planes of weakness would be high leading to delamination.

Delamination is more extensive in the static tensile loading than in impact loading at room temperature. Generally, the stress condition in impact loading should be more severe than that in tensile loading, because of the notch and the high loading speed. The possible explanation may be found in the conditions that exist during the plastic deformation before necking in tensile loading.

The stresses and the rigid zone location in a CVN specimen, however, are much more complex than in a tensile test specimen. As the specimen bends and a plastic zone is generated at the notch, contraction in the thickness direction is constrained, setting up a triaxial stress state. As the crack grows, the location of this zone will move from the area near the notch to spread across most of the fracture surface, which is the reason why delamination evolves as shown in Fig. 2.17 with increase of the tempering temperature. The steel tempered in the range of 500–650 °C has very low strain hardening ability, which leads to low tensile ductility (Song et al. 2006) (Sect. 2.3). Therefore, the stress conditions can easily cause delamination and the anisotropic microstructure (i.e., elongated grains in the triaxial tensile

stress zone) would no doubt separate along the weak paths that are in the plane of hot rolling of the steel, leading to serious delamination. The steel as-rolled, and tempered at 200, 300, 400 and 700 °C, has better elongation-to-failure and the necking ability, resulting in no delamination or only minor local delamination.

The impact specimens tempered at 500–650 °C show no splitting at room temperature, but serious delamination at –30 °C (Table 2.5). In general, the number of delamination increases with a decrease of temperature (Song et al. 2005, 2006; Tsuji et al. 2004). It is well accepted that the yield strength will increase and the elongation-to-failure and the necking ability of steels will be reduced with decreasing temperature. This increase in yield strength can be as much as 10–15 % between room temperature and –30 °C. The stress in the thickness direction needs to be high enough to tear apart the anisotropic microstructure along its weak paths. This is believed to be the reason that delamination is more likely to happen at relatively low temperatures.

Prior plastic strain might induce some microcracks along planes of weakness, which would greatly reduce the required stress for cracks propagation and facilitate the delamination. However, in CVN test the steel has better elongation-to-failure and the necking ability at room temperature and the stress concentration cannot reach that high level.

According to the above analysis, it can also be concluded that the delamination can happen when plane strain condition is satisfied. Correspondingly, the delamination occurs after necking in tensile condition and before the main fracture in impact condition.

It is obvious that the splitting can produce several effects such as strong stress relaxation, reduction of the stress concentration at the main crack tip, promotion of plane stress conditions, i.e. biaxial stress state deep inside the specimen, which could make the delamination more difficult to continue, resulting in ductile fracture. The separated pieces will continue the fracture in the form of the thinner specimens. Local splitting is observed on the surfaces of the separated pieces, as shown in Figs. 2.18a–c. It is reasonable to suggest that this kind of shallow splitting on the primary crack surface should be formed at the same moment as the main splitting occurs due to the necessary strong stress conditions. The ductile fracture on the separated pieces with characteristic dimples may be the last fracture on the main fracture surface.

The steel tempered at 500–650 °C gives similar toughness values at room temperature and at –30 °C (Table 2.5). The fracture appearance and similar toughness values show that –30 °C is above the ductile brittle transition temperature (DBTT). Delamination has no significant influence on the upper shelf energy in the steel. Actually, the continuous splitting can only absorb a little energy, while most of the energy is absorbed by the ductile fracture. Therefore, it is natural that the impact energy is not changed as indicated by comparing the ductile percentages on the fracture surfaces. By comparing the room temperature toughness of the steel as-rolled and the steel tempered at 500–650 °C, the tempering treatment is responsible for the reduction of the toughness.

2.4.7 Summary

Regarding the delamination behaviour of hot-rolled and quenched steel when tensile and impact loaded following tempering at temperatures from 200 to 700 °C, tempering in the range of 500–650 °C leads to serious delamination or splitting during room temperature tensile and –30 °C impact loading. Elongated grains from hot rolling and grain boundary embrittlement resulted from precipitates (alloy carbides and nitrides) formed during tempering are responsible for the delamination. The delamination does not influence the upper shelf impact energy. The number and length of splitting on the low temperature impact fracture surface increase with increase of tempering temperature until 650 °C, and then decrease.

The reasons for the delamination are complex, but can be summarised as the combined effect of the anisotropic microstructure and triaxial stress conditions. The anisotropic microstructure will separate along planes of weakness when the proper plane strain state emerges during the loading. Therefore, the delamination happens after necking in tensile loading and before main fracture in impact loading. Due to the stress–strain behaviour of the steel after tempering in the critical range, delamination is easier under tensile than under impact loading. Decreasing temperature favours delamination, related to the corresponding increase in yield strength and decrease in elongation-to-failure.

References

- Antoine P, Vandeputte S, Vogt JB (2005) Effect of microstructure on strain-hardening behaviour of a Ti-IF steel grade. *ISIJ Int* 45:399–404. doi:[10.2355/isijinternational.45.399](https://doi.org/10.2355/isijinternational.45.399)
- Funakawa Y, Inazumi T, Hosoya Y (2001) Effect of morphological change of carbide on elongation of boron-bearing Al-killed steel sheets. *ISIJ Int* 41:900–907. doi:[10.2355/isijinternational.41.900](https://doi.org/10.2355/isijinternational.41.900)
- Guo Z, Sha W (2004) Kinetics of ferrite to Widmanstätten austenite transformation in a high-strength low-alloy steel revisited. *Z Metallkd* 95:718–723
- Muljono D, Ferry M, Dunne DP (2001) Influence of heating rate on anisothermal recrystallization in low and ultra-low carbon steels. *Mater Sci Eng A* 303:90–99. doi:[10.1016/S0921-5093\(00\)01882-7](https://doi.org/10.1016/S0921-5093(00)01882-7)
- Rivera-Díaz-del-Castillo PEJ, Bhadeshia HKDH (2001) Growth of needle and plate shaped particles: theory for small supersaturations, maximum velocity hypothesis. *Mater Sci Technol* 17:25–29. doi:[10.1179/026708301101509070](https://doi.org/10.1179/026708301101509070)
- Song R, Ponge D, Raabe D (2005) Mechanical properties of an ultrafine grained C-Mn steel processed by warm deformation and annealing. *Acta Mater* 53:4881–4892. doi:[10.1016/j.actamat.2005.07.009](https://doi.org/10.1016/j.actamat.2005.07.009)
- Song R, Ponge D, Raabe D, Speer JG, Matlock DK (2006) Overview of processing, microstructure and mechanical properties of ultrafine grained bcc steels. *Mater Sci Eng A* 441:1–17. doi:[10.1016/j.msea.2006.08.095](https://doi.org/10.1016/j.msea.2006.08.095)
- Sha W (2001) Crystallization and nematic-isotropic transition activation energies measured using the Kissinger method. *J Appl Polym Sci* 80:2535–2537. doi:[10.1002/app.1362](https://doi.org/10.1002/app.1362)
- Tsuji N, Okuno S, Koizumi Y, Minamino Y (2004) Toughness of ultrafine grained ferritic steels fabricated by ARB and annealing process. *Mater Trans* 45:2272–2281. doi:[10.2320/matertrans.45.2272](https://doi.org/10.2320/matertrans.45.2272)

- Yan W, Shan YY, Yang K (2007) Influence of TiN inclusions on the cleavage fracture behavior of low-carbon microalloyed steels. *Metall Mater Trans A* 38A:1211–1222. doi:[10.1007/s11661-007-9161-2](https://doi.org/10.1007/s11661-007-9161-2)
- Yan W, Zhu L, Sha W, Shan YY, Yang K (2009) Change of tensile behavior of a high-strength low-alloy steel with tempering temperature. *Mater Sci Eng A* 517:369–374. doi:[10.1016/j.msea.2009.03.085](https://doi.org/10.1016/j.msea.2009.03.085)
- Yan W, Sha W, Zhu L, Wang W, Shan YY, Yang K (2010) Delamination fracture related to tempering in a high-strength low-alloy steel. *Metall Mater Trans A* 41A:159–171. doi:[10.1007/s11661-009-0068-y](https://doi.org/10.1007/s11661-009-0068-y)
- Yang M, Chao YJ, Li X, Immel D, Tan J (2008) Splitting in dual-phase 590 high strength steel plates: Part II. Quantitative analysis and its effect on Charpy impact energy. *Mater Sci Eng A* 497:462–470. doi:[10.1016/j.msea.2008.07.066](https://doi.org/10.1016/j.msea.2008.07.066)

<http://www.springer.com/978-1-4471-4871-5>

Steels

From Materials Science to Structural Engineering

Sha, W.

2013, XVIII, 268 p., Hardcover

ISBN: 978-1-4471-4871-5